Journal of Solid State Chemistry 314 (2022) 123436

Contents lists available at ScienceDirect

Journal of Solid State Chemistry

journal homepage: www.elsevier.com/locate/jssc

Topochemical intercalation reactions of $ZrSe_3$

Mahmoud Elgaml, Simon J. Cassidy, Simon J. Clarke *

Department of Chemistry, University of Oxford, Inorganic Chemistry Laboratory, South Parks Road, Oxford, OX1 3QR, UK

ARTICLE INFO

Keywords:
Intercalation
Transition metal trichalcogenides
Zirconium triselenide
Stacking faults

ABSTRACT

Intercalation of alkali and alkaline earth metals into $ZrSe_3$ via soft chemical routes injects electrons and has a significant effect on the selenide-selenide bonding. K, Rb and Cs intercalates of $ZrSe_3$ prepared at low temperatures (−78 °C) from metal ammonia solutions contrast with related polymorphs obtained at high temperature (850 °C). K_xZrSe_3 synthesised at low temperatures crystallises in orthorhombic $Cmc2_1$, while the polymorph obtained at high temperatures crystallises in *Immm*. The two structures prepared under drastically different conditions differ by relative shifting of $ZrSe_3$ layers. In contrast, Cs_xZrSe_3 shows the *Immm* polymorph at low temperature and the $Cmc2_1$ polymorph at high temperatures, while a single Rb_xZrSe_3 polymorph in *Immm* is formed at both temperatures. Intercalation of Ca from liquid ammonia facilitates the co-intercalation of the solvent because of the strong solvation of Ca^{2+}. This compound has severe faulting due to the flexibility in the relative shifts of adjacent $ZrSe_3$ layers.

1. Introduction

Transition metal trichalcogenides (TMTCs MCh_3 (M = transition metal; Ch = S, Se, Te) are members of the extensive layered chalcogenide family with the transition metal dichalcogenides (TMDCs, MCh_2) being the most diverse. Early series TMDCs such as TiS_2 contain sulfide ions, S^{2-}, and there is no chalcogenide-chalcogenide bonding [1]. The layered structure and the reducible transition metal enable the Li_xTiS_2 ($0 < x < 1$) system to be used as a prototypical positive electrode material in a Li-ion secondary battery. Other layered TMDCs display a range of desirable properties. For example, MoS_2 is an excellent lubricating material that is also able to catalyse chemical reactions [2,3]. WTe_2 has been shown to exhibit large magnetoresistance and $NbSe_2$ exhibits superconductivity [4,5]. Moving across the periodic table the high oxidation states of the metals become difficult to stabilise and one finds chalcogenide-chalcogenide bonds in MnS_2 and FeS_2 [6] with divalent metal cations and disulfide $[S_2]^{2-}$ ions and the structures are no longer layered.

Although TMTCs are less studied compared to the dichalcogenide variants, it has been proposed that they may have technological potential in optoelectronic, nanoelectronic and photovoltaic applications [7–9]. This is as a result of their structures being viewed as pseudo-one-dimensional [10], offering strong anisotropy in their optical and electrical properties. For example, TiS_3 is a promising candidate for field-effect transistors and photodetectors [11,12]. TiS_3 has also been explored as a potential electrode material in Li- and Na-ion batteries [13]. $ZrTe_3$ has been reported to exhibit superconductivity at ~2 K as well as a charge density wave distortion at 63 K [14–16]. However, intercalations into these layered materials have not been studied in detail despite the investigations of the intercalation chemistry of many other layered chalcogenides driven by research on cathode materials in batteries [17].

$ZrSe_3$ is a member of the group IV trichalcogenide family MCh_3 (M = Ti, Zr, Hf and Ch = S, Se, Te) which all adopt the same $ZrSe_3$ type monoclinic structure with the $P2_1/m$ space group. This layered structure, shown in Fig. 1, consists of $ZrSe_6$ triangular prisms stacked via shared faces to form infinite chains extending along the b axis. These prisms are bi-capped (i.e. capped on two of their rectangular faces), with Zr coordinating to 2 Se in the neighbouring chains. This gives each Zr a coordination number of 8 and forms layers of chains in the ab plane. $ZrSe_3$ is conveniently represented as $Zr^{4+}[Se^{2-}][Se_2]^2$. The $[Se_2]^{2-}$ dimers form the base of the prism and are parallel to the a axis. There is a van der Waals gap between the layers making them suitable candidates for intercalation [18–20].

Lithium intercalation into $ZrSe_3$ was first carried out by Chianelli et al. and subsequently followed up by Sourisseau et al. and Canadell et al. [21–23] It was reported that when chemically intercalating lithium into $ZrSe_3$, three moles of lithium per mole of $ZrSe_3$ were always taken up, corresponding to the full reduction of the chalcogenide to Se^{2-} and reduction of Zr(IV) to Zr(III). The structure appears to have gone through significant change and suffered a substantial loss of crystallinity and hence the structure of this intercalate remains unsolved.

* Corresponding author.
E-mail address: simon.clarke@chem.ox.ac.uk (S.J. Clarke).

https://doi.org/10.1016/j.jssc.2022.123436
Received 6 May 2022; Received in revised form 4 July 2022; Accepted 16 July 2022
Available online 30 July 2022

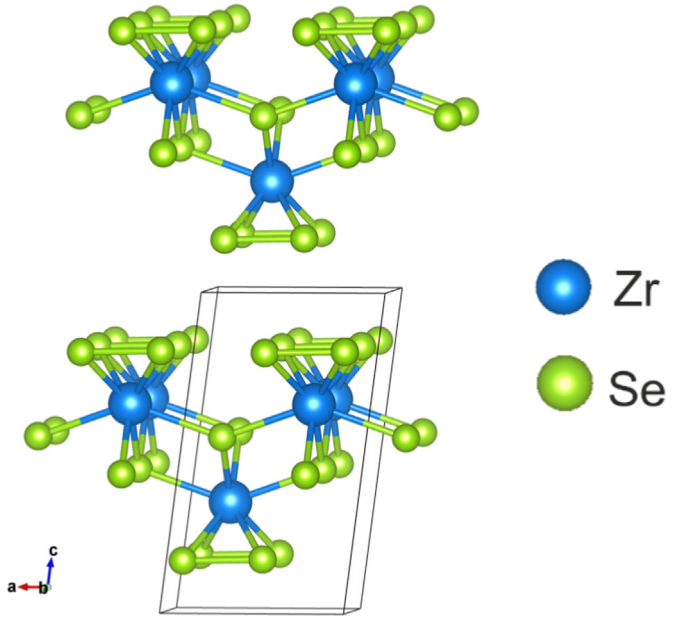

Fig. 1. Structure of $ZrSe_3$ showing that it is formed of layers which are in turn composed of linked $ZrSe_3$ triangular prisms. Se–Se bonds indicate the $[Se_2]^{2-}$ ions.

Klepp et al. reported partially reduced compounds of the form $A_xZr_2Se_6$ ($0.8 < x < 1.1$) with a $ZrSe_3$ framework similar to that in $ZrSe_3$ being formed with group I alkali metal ions, A^+, residing between the layers [24]. Two structures were found which are related to each other by the relative shifting of the $ZrSe_3$ layers. These compounds can formally be described as intercalates of $ZrSe_3$, however, they were not formed in topochemical intercalation reactions, instead they were obtained by reacting A_2Se (A = K, Rb, Cs), Zr and Se in a 1:4:11 ratio at 850 °C. It is particularly notable that these compounds form a similar framework to that found in the binary $ZrSe_3$.

The results reported here show that compositions similar to those obtained by Klepp et al. [24] are also attainable via topochemical reactions of $ZrSe_3$ using low temperature soft chemical methods. Here the structures of the alkali metal (K, Rb and Cs) intercalates are compared with those reported by Klepp et al. [24] and we show that different polymorphs can be attained at low temperatures. Furthermore, the work described here will also show that the use of low temperature intercalation chemistry enables co-intercalation of Ca and ammonia/amide species into this system, leading to a much larger expansion of the interlayer spacing than is found in the alkali metal intercalates.

2. Experimental

2.1. Synthesis

Due to the air sensitivity of the intercalated products, all treatment and handling of materials was carried out in an argon-filled Glovebox Technology dry box or using a Schlenk line. Single-phase crystalline $ZrSe_3$ was synthesised by a direct combination of the elements; zirconium foil (Alfa Aesar, 99.8%) and selenium powder (Alfa Aesar, 99.999%). The starting materials were combined in a dry evacuated silica ampoule and heated at 450 °C for 12 h to ensure reaction of the volatile chalcogen, then heated further at 900 °C for 72 h.

Intercalations of alkali and alkaline earth metal into $ZrSe_3$ were carried using metal/ammonia solutions on a Schlenk line. The Schlenk tube containing approximately 500 mg of $ZrSe_3$ and a 1:1 ratio of the alkali metal and $ZrSe_3$ was evacuated on the Schlenk line and cooled to −78 °C using a solid CO_2/propan-2-ol cooling bath. Approximately 10 cm^3 of ammonia was condensed into the tube via the vacuum line. The solution was left to stir for up to 3 h and warmed to room temperature to enable the ammonia to evaporate off before final evacuation and removal to the dry box. This ratio has the alkali metal in excess to compensate for the difficulty in transferring the metal, especially Rb and Cs, to the Schlenk tube and for any of the metal being slightly oxidised. We assume that any unintercalated metal ions were consumed in side reactions forming amorphous phases, but no crystalline metal amides were detected. (Safety note: ammonia is volatile and highly toxic. At all times venting of the system was available via a mercury manometer attached to the Schlenk line located in a fumehood).

2.2. Structural characterisation

Detailed structural information for the $ZrSe_3$ host and for the intercalated products were obtained from synchrotron powder X-ray diffraction. The data was collected on the I11 beamline at the Diamond Light Source, Harwell, United Kingdom [25]. The synchrotron X-rays were monochromated to have a wavelength of approximately 0.825 Å which was measured accurately at the start of each session of beam time using a silicon standard. Samples were prepared by grinding the material with an equal volume of amorphous silica glass to limit absorption and preferred orientation and packed into flame-sealed 0.5 mm diameter borosilicate capillaries.

Powder neutron diffraction was carried out on the instrument POLARIS at the ISIS pulsed spallation neutron source, Rutherford Appleton Laboratory, United Kingdom [26]. The samples were contained in 6 mm diameter vanadium cans and sealed with indium gaskets. Rietveld analysis was performed using the Topas Academic Version 6 software [27].

3. Results and discussion

3.1. Potassium, rubidium and caesium intercalation

Intercalation of potassium into $ZrSe_3$ using K/NH_3 solution resulted in the black powder turning brown in colour with the dark blue solution of the solvated electrons in ammonia decolourising within minutes. The powder X-ray diffraction pattern showed similarities to that obtained by Klepp et al. with the indexing of the pattern showing an approximate 16% increase in the interlayer separation compared with $ZrSe_3$ itself, and the initial structural model was determined from this literature report. The lattice parameters are in very close agreement with those of the structure of $K_{0.55}ZrSe_3$ reported by Klepp et al. [24] modelled in *Immm*. However, the pattern was fit instead by the $Cmc2_1$ model obtained by them for $Cs_{0.40}ZrSe_3$. This was deduced from the presence of reflections such as 021 and 151 (see Fig. 3) which are symmetry forbidden in *Immm* but allowed in $Cmc2_1$. The two structures are related by different relative shifts of adjacent layers in $ZrSe_3$ as shown in Fig. 2; if the top layer is shifted to the right relative to the bottom layer then an inversion centre appears, the structure has body-centred symmetry and the space group is *Immm*. Whereas if the top layer is shifted to the left as shown in Fig. 2, there is no inversion centre, the structure only has *C*-centring and the space group is non-centrosymmetric $Cmc2_1$. The potassium occupancy refined to 0.45(2) which is 0.1 lower per formula unit than the $K_{0.55}ZrSe_3$ obtained in the high temperature synthesis. In the refinement a single overall displacement parameter was applied to all atoms in reflection of the data quality. Only about half of the potassium in the reaction was incorporated into the host, and we assume that the excess electrons in the metal/ammonia solution are consumed by side reactions. Consistent with this and with the refined composition, we obtained an identical product using 0.5 mol of K per mole of $ZrSe_3$ with a small amount of unconsumed $ZrSe_3$.

Rubidium intercalation using Rb/NH_3 solution proceeded with a similar colour change and a ~20.1% increase in the interlayer separation compared with $ZrSe_3$, This is a ~3.2% (0.385(6) Å) larger increase compared to $K_{0.45(2)}ZrSe_3$, a difference consistent with the greater size of the Rb^+ ion compared with K^+. In contrast to the potassium intercalation,

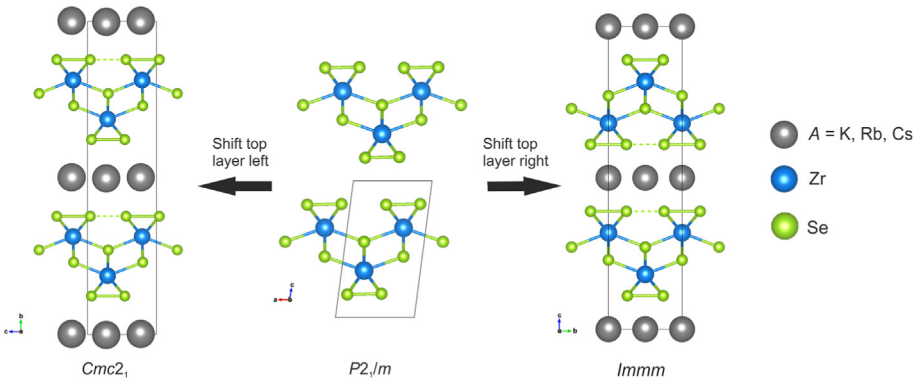

Fig. 2. The relationship between the structure of $ZrSe_3$ (centre) and the structures of the intercalated polymorphs. The dotted line represents the interaction between neighbouring selenide dimers due to their subsequent reduction.

the systematic absences in the diffraction pattern do correspond with those for Klepp et al.'s $Rb_{0.43}ZrSe_3$ *Immm* compound synthesised at high temperatures. The lattice parameters of the rubidium-containing compounds obtained at high temperatures and by direct intercalation are in very close agreement (see Table 1) with only a 0.2% difference in the unit cell volume [24]. The rubidium occupancy in the topotactic intercalation reaction was refined to be 0.41(1) per $ZrSe_3$ unit, again in agreement with the literature value for the high temperature synthesis [24].

Caesium intercalation into $ZrSe_3$ showed an even greater increase of ~24.6% in the interlayer separation. However, comparing this low temperature intercalate to Klepp's $Cs_{0.4}ZrSe_3$ $Cmc2_1$ compound synthesised at high temperature, our low temperature intercalate was found to be ~2.41% (0.284(7) Å) smaller. Moreover, the structure obtained via intercalation crystallises in *Immm* with the structure adopted by the Rb analogues made at high or low temperatures. Again, this was deduced by the absence of the 021 and 151 reflections allowed in $Cmc2_1$ but not in *Immm*; in addition to the presence of the 011 and 013 reflections allowed in *Immm* but not $Cmc2_1$ (see Fig. 3) since they violate the $k = 2n$ reflection condition for 0*kl* reflections. The Cs content refined to 0.42(2) in good agreement with the literature value for the high temperature phase [24]. Due to the difficulty in handling Cs metal, not all the parent $ZrSe_3$ was consumed. Furthermore, a Cs_2Se_3 side product was detected in small amounts possibly due to competing reactions.

In the intercalation reactions, the average Zr–Se distances show no significant change with the values ranging from 2.785(1) - 2.796(2) Å, in good agreement with the 2.7654(2) Å found in $ZrSe_3$. This indicates that the oxidation state of Zr remains at +4. The main change that has occurred is the elongation of the Se–Se dimer distance due to the partial reduction of $[Se_2]^{2-}$. This leads to the subsequent contraction in the distance between neighbouring dimers such that the structures can now be seen as a move away from formal discrete dimers towards a polyselenide chain with alternating Se–Se distances. For $Rb_{0.41(1)}ZrSe_3$ and $Cs_{0.42(1)}ZrSe_3$ crystallising in *Immm*, the selenide dimer bond length has increased from 2.34 Å in $ZrSe_3$ to 2.592 (4) Å and 2.605(5) Å for $Rb_{0.41(1)}ZrSe_3$ and $Cs_{0.42(1)}ZrSe_3$ respectively with the between-dimer distance decreasing from 3.07 Å to 2.775(4) Å and 2.757(5) Å for the Rb and Cs intercalates respectively. The Se–Se distances in these cases with similar electron counts are very similar for both the reported high temperature [24] and our low temperature syntheses.

On the other hand, in $K_{0.45(2)}ZrSe_3$ prepared by intercalation and crystallising in $Cmc2_1$, the selenide dimer bond length has seen an increase to 2.66(1) Å, 0.06(2) Å greater than the distance reported for the *Immm* phase synthesised at high temperatures by Klepp et al. Since the high temperature product $K_{0.55}ZrSe_3$ compound contains slightly more K, which one would expect would cause a larger expansion of the Se–Se dimer distance, it is likely not solely the number of electrons that controls the change of Se dimer length but most likely the different structure as well. In the $Cmc2_1$ phase reported here, the between-dimer Se–Se distance is reduced significantly compared to the value in $ZrSe_3$ and is only an extra 0.06(2) Å longer than the dimer bond length.

Since the reactions were carried out at −78 °C, there is kinetic control over which structure is obtained as opposed to Klepp's high temperature syntheses [24] under thermodynamic control. By considering the coordination environment of the alkali metal in the two different symmetries one can attempt to rationalise why at low temperature the $Cs_{0.42(1)}ZrSe_3$ crystallises in *Immm* similar to $Rb_{0.41(1)}ZrSe_3$.

Table 1
Comparison of the lattice parameters and bond lengths distances of the intercalates. † Values taken from single crystal literature data due to extreme stacking fault leading to difficulty in refining the *x* positions of the selenide dimer in bulk powder. ‡*b* and *c* axes are switched in the $Cmc2_1$ model compared with the *Immm* model.

Compound	Source	Space Group	*a* /Å	*b* /Å	*c* /Å	*β* /°	Volume /Å^3	Interlayer Separation /Å	Van der Waals Gap /Å	Bond Lengths /Å		
										Mean Zr–Se	Se–Se (Dimer)	Se–Se (Non-Dimer)
$ZrSe_3^{\dagger}$	Furuseth *et al.* [28]	$P2_1/m$	5.4109(12)	3.7488(9)	9.444(2)	97.48	189.94	9.444(2)	3.2499(6)	2.7654(2)	2.3441(6)	3.0676(7)
$K_{0.55}ZrSe_3$	Klepp *et al* [24]	*Immm*	3.746(3)	5.354(8)	21.929(3)	90.0	439.8	10.964(2)	4.845(5)	2.763	2.603(2)	2.751(2)
$K_{0.45(2)}ZrSe_3$	This report	$Cmc2_1$	3.76149(9)	21.970(1) ‡	5.3835(1)	90.0	444.90(3)	10.985(1)	4.90(4)	2.789(7)	2.663(10)	2.721(10)
$Rb_{0.43}ZrSe_3$	Klepp *et al.* [24]	*Immm*	3.756(1)	5.359(4)	22.81(1)	90.0	459.1	11.405(5)	5.286(4)	2.771	2.602(3)	2.757(3)
$Rb_{0.41(1)}ZrSe_3$	This report	*Immm*	3.76243(8)	5.3673(1)	22.6882(9)	90.0	458.17(3)	11.344(6)	5.226(5)	2.785(1)	2.592(4)	2.775(4)
$Cs_{0.40}ZrSe_3$	Klepp *et al* [24]	$Cmc2_1$	3.747(1)	24.102(5) ‡	5.332(2)	90.0	481.5	12.051(3)	5.906(4)	2.776	2.572(4)	2.760(4)
$Cs_{0.42(1)}ZrSe_3$	This report	*Immm*	3.76225(7)	5.3616(1)	23.5341(9)	90.0	474.73(3)	11.767(7)	5.580(5)	2.796(2)	2.605(5)	2.757(5)

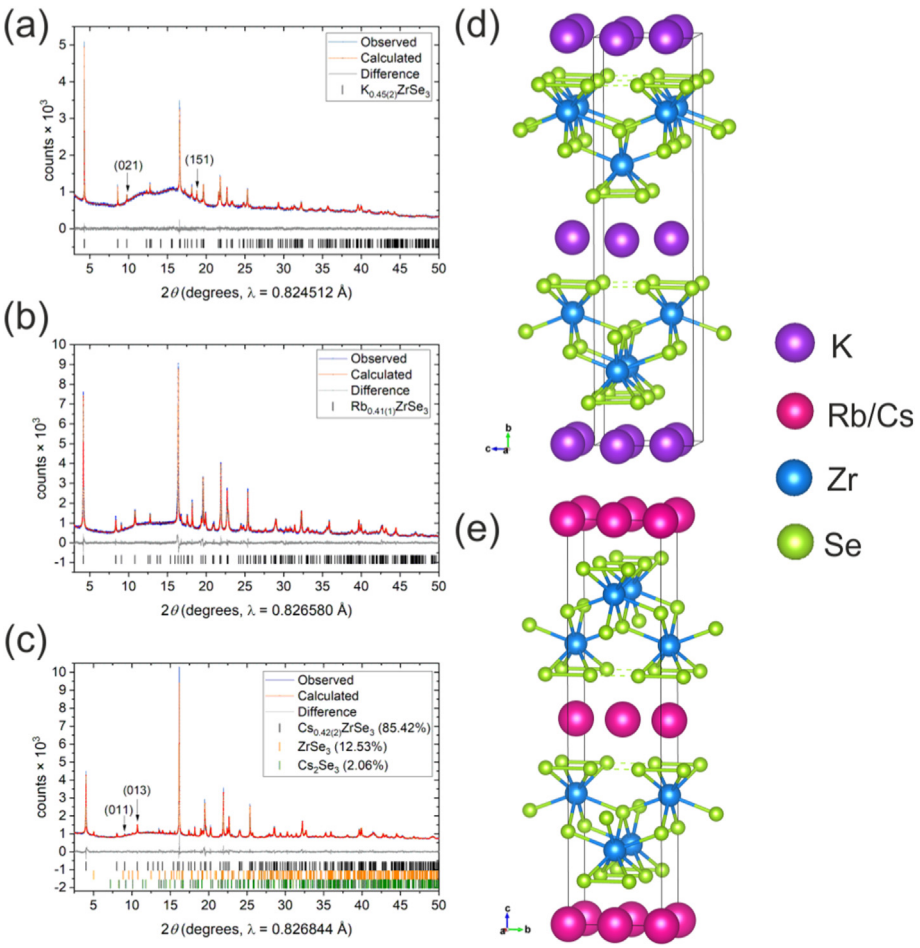

Fig. 3. Rietveld refinement of: (a) $K_{0.45(2)}ZrSe_3$with the 021 and 151 reflections indicated, R_{wp}: 3.05, R_{exp}: 2.88, R_p:2.43, χ^2: 1.12 (b) $Rb_{0.41(1)}ZrSe_3$, R_{wp}: 4.66, R_{exp}: 2.73, R_p 3.50, χ^2: 2.92 and (c) $Cs_{0.42(1)}ZrSe_3$ with the 011 and 013 reflections indicated, R_{wp}: 6.33, R_{exp}: 3.51, R_p 4.89, χ^2: 3.24. (d–e) Structures of the two intercalates.

In the *Immm* structure of $Rb_{0.41(1)}ZrSe_3$ there are two crystallographically distinct alkali metal sites (see Fig. 4). For Rb (1) the ends of the prism are made up from neighbouring selenide dimers contacts of length 2.78 Å whereas for Rb (2) the ends of the prism are made up from the selenide dimers themselves (length 2.59 Å). The different sized prisms are reflected in the Rb fractional occupation of the two sites where Rb(1) and Rb(2) are approximately 0.50 and 0.31 occupied respectively giving an average of 0.41 (similar case for the Cs intercalate). These two sites cannot be simultaneously fully occupied since the repulsion between them will be high. The distance between the sites is ~2.7 Å whereas typical Rb–Rb distances in rubidium chalcogenides and halides such as Rb_2Se and RbCl are 4 Å and 4.65 Å respectively [29,30]. It is

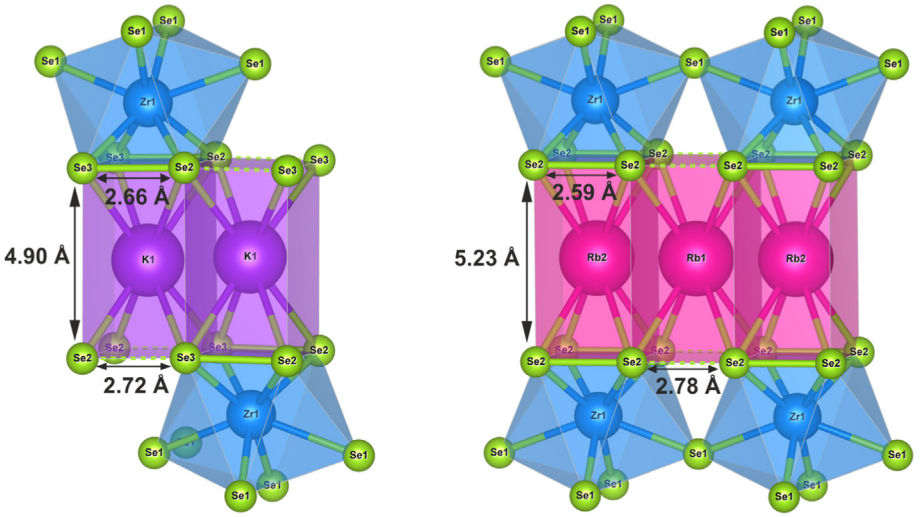

Fig. 4. Comparison of the different alkali metal sites in $Cmc2_1$ (left) and *Immm* (right).

likely that there are large regions within the alkali metal layers where there is a checkerboard-type arrangement of alkali metal ions within a particular layer which would give inter-ion distances of about 4.62 Å, and would be consistent with the mean occupancy of the two sites being below 0.5. However, the absence of any superstructure reflections indicates that there is not full long-range ordering of the alkali ions and vacancies.

In the $Cmc2_1$ structure of $K_{0.45(2)}ZrSe_3$ there is only one crystallographic alkali metal site. One end of the prism is made from the selenide dimer and the other end is made from neighbouring selenide dimers, which are not too dissimilar in length, perhaps to minimise prism distortion. The *Immm* structure therefore contains the largest alkali metal site and this may explain why under kinetic control it is favoured by the large Rb^+ and Cs^+ cations whereas for K^+ this preference is less. In the high temperature *Immm* structure of $K_{0.55}ZrSe_3$, the large cation site allows significantly more K^+ occupation (0.64) giving a mean occupancy for the two sites of slightly above 0.5 according to Klepp et al. [24].

$K_{0.45(2)}ZrSe_3$ was annealed on the I11 synchrotron beamline to test whether the low temperature $Cmc2_1$ can transform into the high temperature *Immm* polymorph. However, upon heating it was found that multiple new peaks at low angles are formed that do not correspond to an *Immm* phase (see Fig. 5). These new peaks could either correspond to decomposition or significant structural rearrangement and could not be indexed. It is plausible that upon heating the low temperature intercalate, other reaction pathways are more favourable than the transformation into the other polymorph.

3.2. Calcium intercalation

The intercalation reaction with a Ca/NH_3 solution resulted in no colour change to the black solid. By modifying the ratio of the reactants and analysing the resultant powder X-ray diffraction pattern it was observed that only 0.2 equivalents of the metal were needed to fully consume the starting material. This is approximately half that required by the alkali metal intercalates, indicating a similar number of electrons donated in forming this product. The complexity of the diffraction pattern will be discussed shortly, but an initial assessment of the structure can be made by observing the position of the 1st 00*l* diffraction peak, which is indicative of the interlayer separation. The interlayer separation of this product of nominal composition '$Ca_{0.2}ZrSe_3$' is 10% greater than that of the $K_{0.45(2)}ZrSe_3$ intercalate, which strongly suggests that co-intercalation of the solvent has also occurred. Chemical analysis (Elemental Microanalysis Ltd, Okehampton, UK: CHN using the Dumas combustion method) confirmed the presence of ammonia/amide species with a N:H ratio of 1:2.77(8) and gave 0.596(7) N per formula unit which suggests a formula of $Ca_{0.2}(NH_3)_{0.45(7)}(NH_2)_{0.15(7)}ZrSe_3$. Using this approximation, the $[Se_2]^{2-}$ dimer would be slightly less reduced compared to the alkali intercalates as only 0.25(7) electrons (instead of ~0.4) are used in the reduction with the remaining electrons used to form H_2 during the reduction of NH_3 to form NH_2^-.

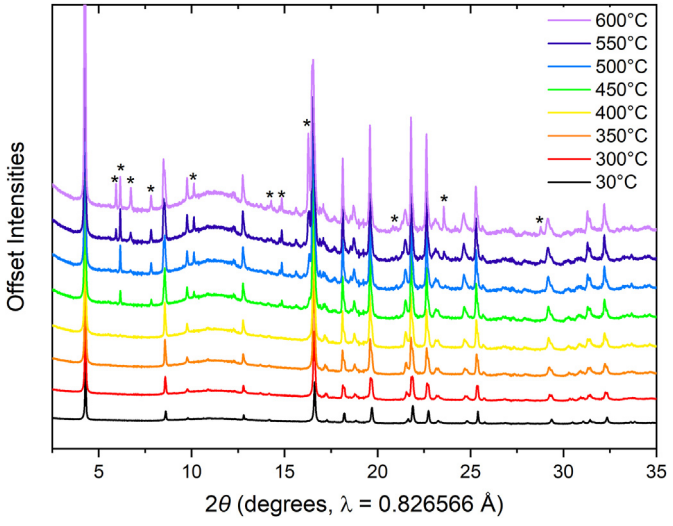

Fig. 5. Synchrotron XRD patterns of the *in situ* heating of $K_{0.45(2)}ZrSe_3$. The asterisks indicate the new peaks formed.

Unlike the alkali metal intercalates, the structure was not trivial to characterise. An initial model was based on the *Immm* structure of $K_{0.55}ZrSe_3$ with expanded lattice parameters, which accounted well for the peak positions and gave a satisfactory fit to the powder X-ray diffraction if a suitably broad and anisotropic peak shape model was used. However, this model struggled to account for the intensities of low *d*-spacing reflections which is particularly evident in the powder neutron diffraction where these reflections are better resolved (see Fig. S1).

A combination of sharp and broad peaks in both the synchrotron X-ray and neutron diffraction patterns are consistent with significant stacking disorder. Topas Academic Version 6 was used to account for this. Without a clear knowledge of the types of stacking disorder involved it was not feasible to construct a model based on a small number of additional parameters such as those previously reported in the literature [31–33]. Microscopy techniques such as HAADF-STEM imaging in principle provide insight to the types of stacking disorder present, but ammonia-intercalated layers are typically unstable with respect to an electron beam. We modelled the stacking disorder present in $Ca_{0.2}(NH_3)_{0.45(7)}(NH_2)_{0.15(7)}ZrSe_3$ without any existing knowledge of the type of stacking disorder present in the following way. The initial *Immm* structure giving the fits shown in Fig. S1 was separated into $ZrSe_3$ and Ca/NH_3 subunits, the divide between the blocks chosen to be at the centre of the van der Waals gap. The *Immm* structure may thus be regenerated by a stacking model containing two of the $ZrSe_3$ and Ca/NH_3 subunits, with a ½, ½ offset in the *ab* plane applied to the second pair of subunits to account for the body-centring in the *Immm* structure. We then generated a supercell by stacking 100 $ZrSe_3$ subunits with 100 intervening Ca/NH_3 subunits, with suitable offsets to mimic the body-centring.

This initial large supercell thus corresponds exactly to the *Immm* structure. Instead of refining this model using anisotropic peak broadening, we used a simple symmetric peak shape based on isotropic crystallite size broadening of the peaks and the relative positions of the subunits were then refined, with the 1st $ZrSe_3$ subunit remaining fixed as an anchor. This positional refinement of the subunits was first attempted by only allowing them to vary in the *ab* plane – modelling turbostratic disorder/variation in the structure. Refinements of the relative shifts in the *a*-direction (i.e. along the axis of the $ZrSe_6$ prisms) always led to negligible shifting whereas the shifting in the *b* direction (parallel to the axis of the Se dimers) was significant. Allowing both the $ZrSe_3$ and Ca/NH_3 subunits to refine their position in just the *b*-direction (Fig. S2) leads to R_{wp} for the neutron diffraction improving from 7.1% to 4.6% in the 90° data bank. Due to the size of the refinement and number of peaks calculated, it was only practically possible to refine against one bank of the neutron data at a time for the stacking model. It is reasonable to be suspicious of a model that allows hundreds of freely refining parameters, and indeed many different absolute configurations of the supercell can give equivalent fits to the data. However, all solutions of equivalent R_{wp} give the same distribution of relative shifts from one $ZrSe_3$ subunit to the next (Fig. S3), which is reproduced across both the X-ray and neutron diffraction refinements as shown in Fig. 7(c–d).

The consequence of this result can be understood by relating it to the $Cmc2_1$ and *Immm* models which are shown in Fig. 2. For the pure *Immm* model the distribution of relative shifts in Fig. 7(c) would have a single sharp peak at 0, whereas for the pure $Cmc2_1$ model there would be symmetric sharp peaks at ±0.5. The model produced by our stacking fault analysis has a large degree of variability in the *b*-direction shift, with a broad peak centred around 0 and no secondary maxima at ±0.5, suggesting that on average the $ZrSe_3$ subunits remain in the body-centred *Immm* configuration, consistent with the initial indexing of the pattern.

Comparing the Ca/NH_3 subunit *b*-axis shift relative to the $ZrSe_3$ subunits above and below it in Fig. S4 shows a clear preference for shifts of (0, 0), (±0.5, ±0.5), (0, ±0.5) and (±0.5, 0). This is summarised in the distribution diagram in Fig. 7(d) showing the average of the modulus of the shifts. A shift of 0 indicates that the arrangement of Ca/NH_3 and $ZrSe_3$ subunits remains unmoved from the initial *Immm* model. A 0.5 shift suggests the Ca/NH_3 subunit shifting by half a unit cell such that the Ca and the NH_3 have swapped positions whilst the $ZrSe_3$ subunits remain unchanged. A shift of 0.25, an average of 0 and 0.5, suggests that one of the $ZrSe_3$ subunits either above or below the Ca/NH_3 subunit has shifted by half a unit cell. The two adjacent $ZrSe_3$ subunits therefore take up the arrangement as in the $Cmc2_1$ model. Both X-ray and neutron distributions show peaks at 0 and 0.5 indicating the majority preference of the *Immm* arrangement. Both the X-ray and neutron models show a higher frequency of 0 shifts than 0.5 shifts, indicating the Ca and NH_3 have a higher preference for their assigned positions as shown in Fig. 6, rather than being interchanged. The distribution in the X-ray model shows a lower preference for Ca/NH_3 ordering than the neutron, which is expected due to the lower contrast between the X-ray form factors of 0.2 Ca and 0.6 N with respect to the neutron scattering lengths (Ca: 4.70 fm, H: −3.74 fm, N: 9.36 fm) [34]. This result supports the initial, intuitive assignment of the two sites, in which NH_3 has a closer proximity to Se to allow for increased Se···H hydrogen bonding.

A further improvement to the fit can be achieved by allowing the subunits to move relative to one another in the stacking direction, *c*. The bond lengths and contents of the layers were kept constant but their relative positions along *c* were refined, effectively increasing or decreasing the van der Waals gaps between them, which provides a rough modelling of interstratification (i.e. the variation/disorder between alternate layers) in a structure. In this case the modelling accounts for different amounts of intercalation leading to different interlayer separations from one layer to the next. The $ZrSe_3$ subunit *c* shifts were refined while the Ca/NH_3 *c* shifts were constrained such that each subunit stayed in the centre of the van der Waals gap of the $ZrSe_3$ subunits above and below it. The R_{wp} of the neutron fit improves significantly from 4.6% to 1.7% on inclusion of this variation, providing the fit to the data shown in Fig. 7(b).

The improvement of the fit on addition of interstratification to the model clearly shows that the distribution of the calcium-ammonia/amide co-intercalant between the $ZrSe_3$ layers is non-uniform across the crystallites. Some variation of this kind is plausible, and once again is reproduced by separate models to both the X-ray and neutron diffraction data as shown in Fig. 7(e), giving similar distributions of different interlayer separations. There were no obvious correlations between turbostraticity and interstratification, but correlations may be present outside the detection limits of the model.

This method of stacking fault refinement provides insight into the type and degree of disorder in the structure, but the model does come with limitations. The method of modelling interstratification is limited by the constraint that for every expanded layer there must be a contracted layer to match – so it is plausible that the true distribution of interlayer spacings is not well represented. While it is possible to refine the bond distances and atomic site occupancies, these are realistically likely to be too correlated to shifting parameters to be confidently extracted and so it is necessary to fix them to sensible values. To best approximate these bond distances, the atomic coordinates for the layers were taken from the initial refinement based on the *Immm* model. This gave a Se–Se distance in the $ZrSe_3$ layer of ~2.52 Å and ~2.83 Å for the dimer and non-dimer distances respectively, consistent with the fact that the selenide dimer was less reduced compared to the alkali intercalates due to the presence of amide species. Since 0.2 equivalents of Ca^{2+} per $ZrSe_3$ were used in the synthesis and chemical analysis suggests 80% occupancy overall of the two sites occupied by alkali metals in Fig. 4, Ca was modelled with an occupancy of 0.2 on one of the cation sites with N occupancy of 0.6 on the other site. This would give a Ca–N distance of ~2.67 Å which is reasonable as a typical Ca–N distance such as in calcium imide is 2.57 Å [35].

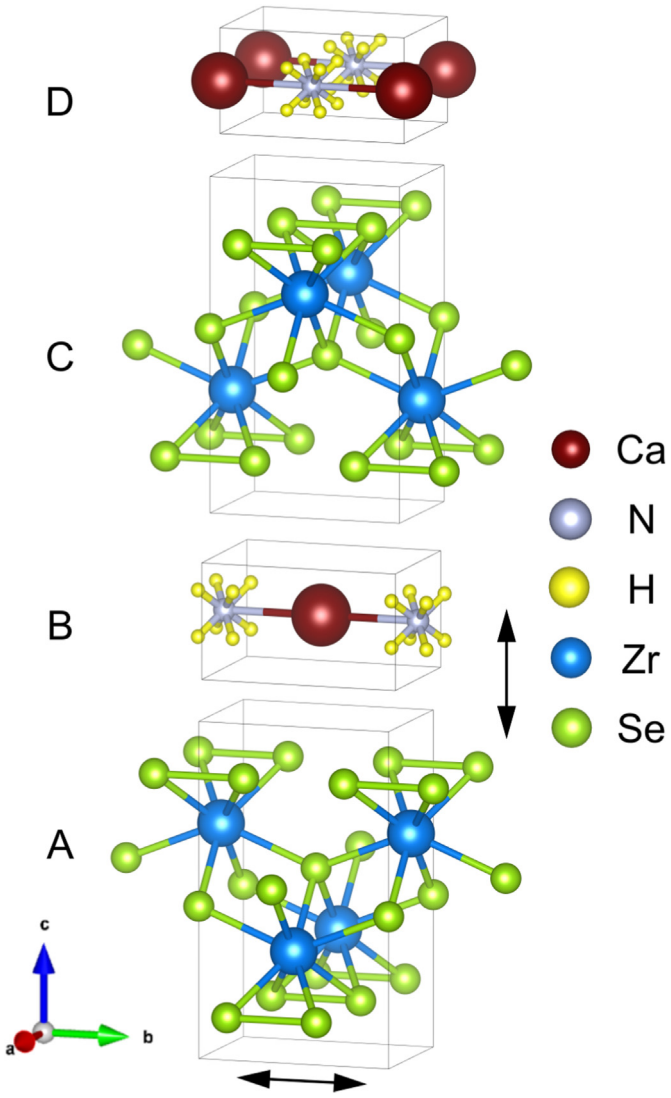

Fig. 6. Subunits A-D of $ZrSe_3$ and Ca/NH_3 based off *Immm* used in stacking model. The arrows indicate the directions that the subunits were allowed to refine.

The hydrogen positions in the neutron refinement were approximated to have a square prismatic coordination around N with a bond length ~1 Å giving 8 potential N–H···Se hydrogen bonds with a distance of 2.7–2.8 Å as seen in other metal/ammonia intercalates [36,37]. The H content calculated from the elemental analysis was split across the 8 sites. These constraints were necessary to implement the stacking fault modelling but some are expected to be non-physical, for example it is plausible that the Se–Se distances take a range of values rather than just two, and it is expected that the Ca/NH_3 occupancies will vary with the differing interlayer separations whereas they are all taken to be identical in the model. Nevertheless, the necessity to include both turbostratic and interstratification disorder in order to accurately fit the diffraction data allows us to be confident that both types of stacking disorder are present.

The variation in the *b*-axis shift seen in this intercalate but not in alkali metals intercalates might be explained by the role of ammonia/amide. Unlike in the alkali metal variants, the interlayer spacing is too large for the small Ca^{2+} intercalant to be involved in any significant bonding interaction with the selenide ions – the Ca^{2+} ions remain solvated by the ammonia and amide moieties which interact with the selenide ions, presumably by N–H···Se hydrogen bonding interactions as found in other metal/ammonia intercalates [36,37]. The layers are thus not 'locked' in position by bonding to the intercalant cation and there is

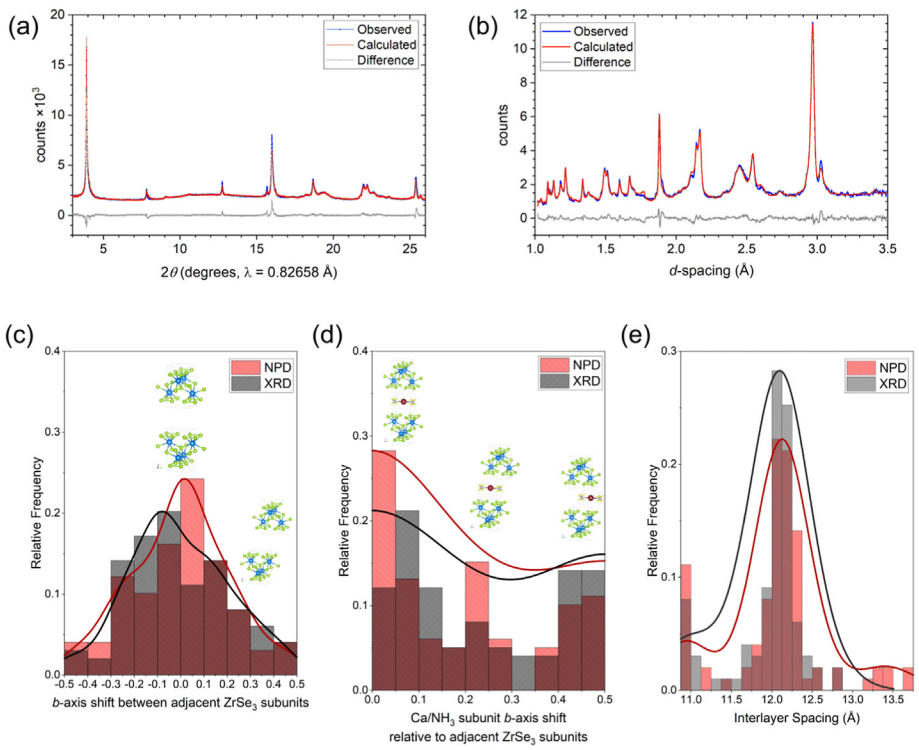

Fig. 7. (a) X-ray powder diffraction pattern of $Ca_{0.2}(NH_3)_{0.45(7)}(NH_2)_{0.15(7)}ZrSe_3$, R_{wp}: 7.51, R_{exp}: 2.25, R_p: 5.31, χ^2: 11.09. (b) Neutron powder diffraction pattern of $Ca_{0.2}(NH_3)_{0.45(7)}(NH_2)_{0.15(7)}ZrSe_3$. R_{wp}: 1.70, R_{exp}: 16.30, R_p: 1.20, χ^2: 0.01 [note that the large R_{exp} and low χ^2 for the refinement against POLARIS data is a consequence of the scaling applied to the multibank refinement]. (c) Distribution of coordinate shifts between adjacent $ZrSe_3$ subunits in the *b*-axis. (d) Distribution of *b*-axis shifts of the Ca/NH_3 subunit relative to adjacent $ZrSe_3$ subunits. (e) Distribution of the interlayer spacing. Trace lines in (c–e) are kernel density smooth lines.

more freedom in their relative arrangement compared with the alkali intercalates.

3.3. Raman spectroscopy

Raman spectroscopy measurements were carried out on a Thermo Scientific DXR3 SmartRaman Spectrometer using 785 nm radiation. The parent $ZrSe_3$ displays the main modes as previously reported [38]. Only the A_g^8 mode is exclusive to the $[Se_2]^{2-}$ dimer (Fig. 8(b)) with the A_g^3, A_g^5 and A_g^6 modes involving the Zr and the Se^{2-} as well.

Comparing the Raman spectra of the intercalates it is evident that intercalation and the consequence reduction of the $[Se_2]^{2-}$ dimer has a significant effect on the modes. This is especially seen when looking at the A_g^8 mode which disappears when intercalating alkali metals but remains for the Ca/NH_3 intercalate. Lengthening of the Se–Se dimer would be expected to cause a shift to a much lower wavenumber. It is plausible that the new peak seen at 200 cm^{-1} is the shifted A_g^8 mode due to a reduced selenide. The presence of both this new peak and the unshifted

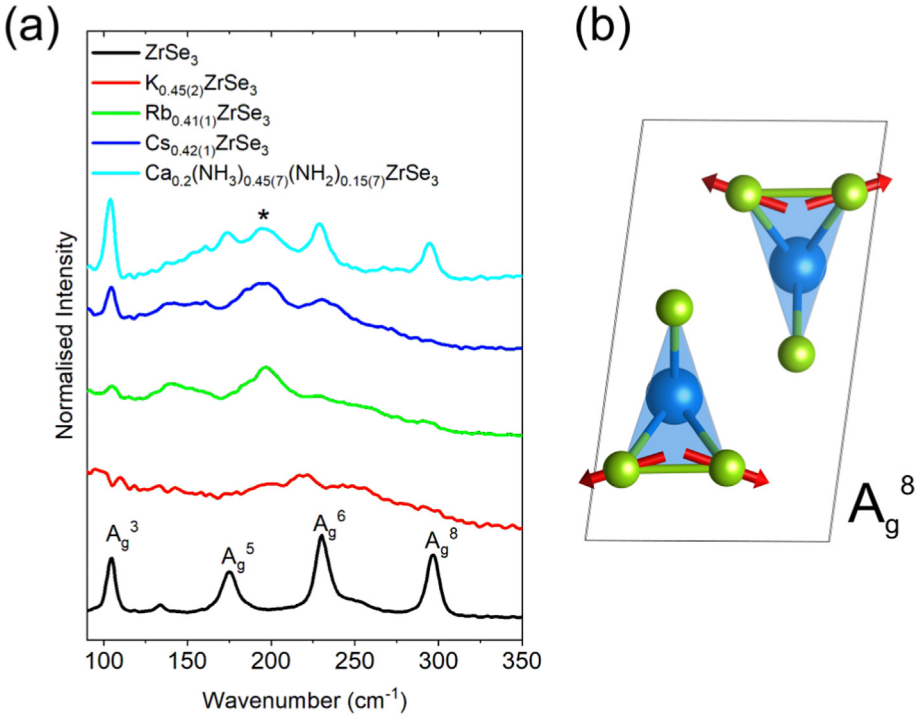

Fig. 8. (a) Raman spectra of $ZrSe_3$ and its intercalates. (b) Schematic of the A_g^8 Raman mode. The asterisk indicates the new peak.

Table 2
Molar susceptibility (χ_{mol}) values of $ZrSe_3$ and its intercalates.

Compound	χ_{mol} ($\times 10^{-5}$ emu mol^{-1})
$ZrSe_3$	−8.17(1)
$K_{0.45(2)}ZrSe_3$	−7.33(1)
$Rb_{0.41(1)}ZrSe_3$	−9.67(1)
$Cs_{0.42(1)}ZrSe_3$	−7.76(2)
$Ca_{0.2}(NH_3)_{0.45(7)}(NH_2)_{0.15(7)}ZrSe_3$	−8.15(2)

A_g^8 mode in the Ca/NH_3 intercalate may suggest that some of the dimers are reduced and some are not, instead of a uniform partial reduction. Therefore the ~2.52 Å dimer length used in the stacking fault refinement may in effect be an average of reduced and non-reduced dimers. Using 2.6 Å as an approximate reduced dimer length (based on the alkali intercalates) and 2.34 Å as the non-reduced dimer length (based on parent $ZrSe_3$), an average of 2.52 Å would correspond to 69% reduced dimers. Given that for the alkali metal intercalates ~0.4 electrons would achieve uniform reduced dimers, the 0.25 (7) electrons available for reduction (from elemental analysis) would correspond to 45–80% reduced dimers hence 69% falls within this range.

The presence of non-reduced dimers would support the theory that some of the Se dimers do not have any significant bonding interaction with the Ca^{2+} intercalant; therefore, the layers are free to move hence why significant stacking disorder is present in this system. This however does not rule out the possibility of some hydrogen bonding of the NH_3/NH_2^- species to Se as seen in the Li/NH_3 intercalation of FeSe [36].

3.4. SQUID magnetometry

Magnetic susceptibility measurements were measured on the Quantum Design MPMS-3 SQUID magnetometer. The magnetisation was measured against a magnetic field varying from 0 to 5 T at 300 K using 20 mg of sample in a gelatin capsule. The host $ZrSe_3$ shows a clear diamagnetic signal with a molar susceptibility (χ_{mol}) of $-8.17\ (1)\times10^{-5}$ emu mol^{-1}. The intercalates also remain diamagnetic with χ_{mol} varying only by $\pm2\times10^{-5}$ emu mol^{-1} (Table 2). This confirms the nature of the reduction in that the Zr^{4+} oxidation state remains unchanged and that therefore the reduction is taking place in the $[Se_2]^{2-}$ dimers.

4. Conclusion

The work presented here has shown that the low temperature intercalation into $ZrSe_3$ occurs producing differing polymorphs to those previously reported in a high temperature synthesis. Under these conditions, the reactions are under kinetic control and it therefore likely that the polymorphs found for the Rb and Cs intercalates are dictated by the large size of the cations preferring to occupy the largest site possible which is found in the *Immm* structure. Annealing the low temperature $Cmc2_1$ K intercalate appeared to favour other reaction pathways than the transformation into the high temperature *Immm* polymorph.

The intercalation with Ca proceeds with co-intercalation of the ammonia solvent. This results in an expansion that is greater than that of the Cs intercalate. Elemental analysis confirms the presence of the solvent species and suggests a formula of $Ca_{0.2}(NH_3)_{0.45(7)}(NH_2)_{0.15(7)}ZrSe_3$. The co-intercalation resulted in large interlayer separations such that the compound suffers from severe stacking disorder due to the alkaline earth metal ion having little bonding interaction with the Se. The diffraction patterns cannot be simply modelled with either the *Immm* or $Cmc2_1$ models, therefore a stacking fault model based on the *Immm* model was used where multiple rigid blocks of $ZrSe_3$ and Ca/NH_3 were allowed to refine independently. This model significantly improved the fit to the observed X-ray and neutron diffraction patterns with the body-centred *Immm*-type arrangement of $ZrSe_3$ layers having the largest probability. Ca/NH_3 layer shifts in the neutron refinement show a clear favourability of the NH_3 being in closer proximity to the Se presumably to facilitate hydrogen bonding. Raman spectroscopy showed the presence of the non-reduced selenide dimer (A_g^8) mode as well as a new peak at lower wavenumber which may correspond to the lengthening of selenide dimers. This would suggest that in this system there is a mixture of reduced and non-reduced dimers rather than a uniform partial reduction as found in the alkali metal intercalates and this is consistent with the chemical analysis.

CRediT authorship contribution statement

Mahmoud Elgaml: synthesised the samples, carried out the analysis and wrote the paper. **Simon J. Cassidy:** Analysis of the stacking fault refinement. **Simon J. Clarke:** provided materials and initial concepts.

Declaration of competing interest

The authors declare that they have no known competing financial interests or personal relationships that could have appeared to influence the work reported in this paper.

Data availability

Data will be made available on request.

Acknowledgements

We thank: the Leverhulme Trust (RPG-2018-377) and the UK EPSRC (EP/T027991/1, EP/R042594/1 and EP/P018874/1) for funding; the ISIS Pulsed Neutron and Muon Source (RB1920112) and the Diamond Light Source Ltd (EE18786 and CY25166) for the award of beam time. We thank Dr. R. I. Smith for support on POLARIS, Dr A. Baker and Dr C. Murray for support on I11 and E. Yang for assistance with the Raman Spectrometer.

Appendix A. Supplementary data

Supplementary data to this article can be found online at https://doi.org/10.1016/j.jssc.2022.123436.

References

[1] R.R. Chianelli, J.C. Scanlon, A.H. Thompson, Structure refinement of stoichiometric TiS_2, Mater. Res. Bull. 10 (1975) 1379–1382, https://doi.org/10.1016/0025-5408(75)90100-2.
[2] P.D. Fleischauer, R. Bauer, Chemical and structural effects on the lubrication properties of sputtered MoS_2 films, Tribol. Trans. 31 (1988) 239–250, https://doi.org/10.1080/10402008808981819.
[3] Y. Li, H. Wang, L. Xie, Y. Liang, G. Hong, H. Dai, MoS2 nanoparticles grown on graphene: an advanced catalyst for the hydrogen evolution reaction, J. Am. Chem. Soc. 133 (2011) 7296–7299, https://doi.org/10.1021/ja201269b.
[4] M.N. Ali, J. Xiong, S. Flynn, J. Tao, Q.D. Gibson, L.M. Schoop, T. Liang, N. Haldolaarachchige, M. Hirschberger, N.P. Ong, R.J. Cava, Large, non-saturating magnetoresistance in WTe_2, Nature 514 (2014) 205–208, https://doi.org/10.1038/nature13763.
[5] R.C. Morris, R.V. Coleman, R. Bhandari, Superconductivity and magnetoresistance in $NbSe_2$, Phys. Rev. B 5 (1972) 895–901, https://doi.org/10.1103/PhysRevB.5.895.
[6] G. Brostigen, A. Kjekshus, E.E. Astrup, V. Nordal, A.A. Lindberg, J.C. Craig, Redetermined crystal structure of FeS_2 (pyrite), Acta Chem. Scand. 23 (1969) 2186–2188, https://doi.org/10.3891/acta.chem.scand.23-2186.
[7] Y. Jin, X. Li, J. Yang, Single layer of MX_3 (M = Ti, Zr; X = S, Se, Te): a new platform for nano-electronics and optics, Phys. Chem. Chem. Phys. 17 (2015) 18665–18669, https://doi.org/10.1039/c5cp02813b.
[8] W. Kong, C. Bacaksiz, B. Chen, K. Wu, M. Blei, X. Fan, Y. Shen, H. Sahin, D. Wright, D.S. Narang, S. Tongay, Angle resolved vibrational properties of anisotropic transition metal trichalcogenide nanosheets, Nanoscale 9 (2017) 4175–4182, https://doi.org/10.1039/c7nr00711f.
[9] J. Dai, X.C. Zeng, Titanium trisulfide monolayer: theoretical prediction of a new direct-gap semiconductor with high and anisotropic carrier mobility, Angew. Chemie - Int. Ed. 54 (2015) 7572–7576, https://doi.org/10.1002/anie.201502107.
[10] J.O. Island, A.J. Molina-Mendoza, M. Barawi, R. Biele, E. Flores, J.M. Clamagirand, J.R. Ares, C. Sánchez, H.S.J. Van Der Zant, R. D'Agosta, I.J. Ferrer, A. Castellanos-Gomez, Electronics and optoelectronics of quasi-1D layered transition metal trichalcogenides, 2D Mater. 4 (2017), 022003, https://doi.org/10.1088/2053-1583/aa6ca6.

[11] J.O. Island, R. Biele, M. Barawi, J.M. Clamagirand, J.R. Ares, C. Sánchez, H.S.J. Van Der Zant, I.J. Ferrer, R. D'Agosta, A. Castellanos-Gomez, Titanium trisulfide (TiS_3): a 2D semiconductor with quasi-1D optical and electronic properties, Sci. Rep. 6 (2016) 1–7, https://doi.org/10.1038/srep22214.
[12] J.O. Island, M. Buscema, M. Barawi, J.M. Clamagirand, J.R. Ares, C. Sánchez, I.J. Ferrer, G.A. Steele, H.S.J. van der Zant, A. Castellanos-Gomez, Ultrahigh photoresponse of few-layer TiS_3 nanoribbon transistors, Adv. Opt. Mater. 2 (2014) 641–645, https://doi.org/10.1002/ADOM.201400043.
[13] J. Wu, D. Wang, H. Liu, W.M. Lau, L.M. Liu, An ab initio study of TiS_3: a promising electrode material for rechargeable Li and Na ion batteries, RSC Adv. 5 (2015) 21455–21463, https://doi.org/10.1039/c4ra15055d.
[14] S. Takahashi, T. Sambongi, J.W. Brill, W. Roark, Transport and elastic anomalies in $ZrTe_3$, Solid State Commun. 49 (1984) 1031–1034, https://doi.org/10.1016/0038-1098(84)90416-2.
[15] H. Nakajima, K. Nomura, T. Sambongi, Anisotropic superconducting transition in $ZrTe_3$, Phys. B+C 143 (1986) 240–242, https://doi.org/10.1016/0378-4363(86)90106-3.
[16] D.J. Eaglesham, J.W. Steeds, J.A. Wilson, Electron microscope study of superlattices in $ZrTe_3$, J. Phys. C Solid State Phys. 17 (1984) L697–L698, https://doi.org/10.1088/0022-3719/17/27/001.
[17] M.S. Whittingham, Electrical energy storage and intercalation chemistry, Science 192 (1976) 1126–1127, https://doi.org/10.1126/science.192.4244.1126.
[18] W. Krönert, K. Plieth, Zur Kristallstruktur des $ZrSe_3$, Naturwissenschaften 45 (1958) 416, https://doi.org/10.1007/BF00603229.
[19] W. Krönert, K. Plieth, Die Struktur des Zirkontriselenids $ZrSe_3$, ZAAC - J. Inorg. Gen. Chem. 336 (1965) 207–218, https://doi.org/10.1002/zaac.19653360311.
[20] L. Brattas, A. Kjekshus, On the properties of Compounds with the $ZrSe_3$ type structure, Acta Chem. Scand. 26 (1972) 3441–3449, https://doi.org/10.3891/acta.chem.scand.26-3441.
[21] C. Sourisseau, S.P. Gwet, P. Gard, Y. Mathey, Structural, optical and electronic properties of Li_3MX_3 compounds (M = Ti, Zr, Hf), J. Solid State Chem. 211 (1988) 257–271. https://www.sciencedirect.com/science/article/pii/0022459688900291.
[22] E. Canadell, C. Thieffry, Y. Mathey, M.H. Whangbo, Energy factors governing the partial irreversibility of lithium intercalation in layered trichalcogenides MX_3 (M = Ti, Zr, Hf; X = S, Se) and the structural changes in the intercalated species Li_3MX_3, Inorg. Chem. 28 (1989) 3043–3047, https://doi.org/10.1021/ic00314a035.
[23] R.R. Chianelli, M.B. Dines, Reaction of n-butyllithium with transition metal trichalcogenides, Inorg. Chem. 14 (1975) 2417–2421, https://doi.org/10.1021/ic50152a023.
[24] K.O. Klepp, N.A. Harringer, A. Kolb, $K_{1.10}Zr_2Se_6$, $Rb_{0.86}Zr_2Se_6$ and $Cs_{0.80}Zr_2Se_6$. The first intercalation compounds of zirconium triselenide, Z. Naturforsch. B Chem. Sci. 57 (2002) 1265–1269, https://doi.org/10.1515/znb-2002-1111.
[25] S.P. Thompson, J.E. Parker, J. Potter, T.P. Hill, A. Birt, T.M. Cobb, F. Yuan, C.C. Tang, Beamline I11 at Diamond: a new instrument for high resolution powder diffraction, Rev. Sci. Instrum. 80 (2009), 075107, https://doi.org/10.1063/1.3167217.
[26] R.I. Smith, S. Hull, M.G. Tucker, H.Y. Playford, D.J. McPhail, S.P. Waller, S.T. Norberg, The upgraded Polaris powder diffractometer at the ISIS neutron source, Rev. Sci. Instrum. 90 (2019), 115101, https://doi.org/10.1063/1.5099568.
[27] A.A. Coelho, TOPAS and TOPAS-Academic: an optimization program integrating computer algebra and crystallographic objects written in C++: an, J. Appl. Crystallogr. 51 (2018) 210–218, https://doi.org/10.1107/S1600576718000183.
[28] S. Furuseth, L. Brattås, A. Kjekshus, A.F. Andresen, P. Fischer, On the Crystal Structures of TiS_3, ZrS_3, $ZrSe_3$, $ZrTe_3$, HfS_3, and $HfSe_3$, Acta Chem. Scand. 29a (1975) 623–631, https://doi.org/10.3891/acta.chem.scand.29a-0623.
[29] H. Sommer, R. Hoppe, Die Kristallstruktur von Cs2S. mit einer Bemerkung über Cs_2Se, Cs_2Te, Rb_2Se und Rb_2Te, ZAAC - J. Inorg. Gen. Chem. 429 (1977) 118–130, https://doi.org/10.1002/zaac.19774290116.
[30] F.F.Y. Wang, D.E. Cox, The coherent neutron scattering amplitude of Rb: a neutron diffraction study of RbCl, Acta Crystallogr. A 26 (1970) 377–379, https://doi.org/10.1107/S0567739470000906.
[31] C.M. Ainsworth, J.W. Lewis, C.H. Wang, A.A. Coelho, H.E. Johnston, H.E.A. Brand, J.S.O. Evans, 3D transition metal ordering and rietveld stacking fault quantification in the new oxychalcogenides $La_2O_2Cu_{2-4x}Cd_{2x}Se_2$, Chem. Mater. 28 (2016) 3184–3195, https://doi.org/10.1021/acs.chemmater.6b00924.
[32] S.J. Cassidy, M.J. Pitcher, J.J.K. Lim, J. Hadermann, J.P. Allen, G.W. Watson, S. Britto, E.J. Chong, D.G. Free, C.P. Grey, S.J. Clarke, Layered CeSO and LiCeSO oxide chalcogenides obtained via topotactic oxidative and reductive transformations, Inorg. Chem. 58 (2019) 3850, https://doi.org/10.1021/acs.inorgchem.8b03485.
[33] S. Bette, R.E. Dinnebier, 2 Understanding stacking disorder in layered functional materials using powder diffraction, in: S. Schorr, C. Weidenthaler (Eds.), Crystallogr. Mater. Sci. From Struct. Relationships to Eng., De Gruyter, 2021, pp. 55–92, https://doi.org/10.1515/9783110674910-002.
[34] V.F. Sears, Neutron scattering lengths and cross sections, Neutron News 3 (1992) 26–37, https://doi.org/10.1080/10448639208218770.
[35] T. Sichla, H. Jacobs, Synthesis and crystal structure of calcium imide, CaNH, Zeitschrift Fur Anorg. Und Allg. Chemie. 622 (1996) 2079–2082, https://doi.org/10.1002/zaac.19966221214.
[36] M. Burrard-Lucas, D.G. Free, S.J. Sedlmaier, J.D. Wright, S.J. Cassidy, Y. Hara, A.J. Corkett, T. Lancaster, P.J. Baker, S.J. Blundell, S.J. Clarke, Enhancement of the superconducting transition temperature of FeSe by intercalation of a molecular spacer layer, Nat. Mater. 12 (2013) 15–19, https://doi.org/10.1038/nmat3464.
[37] M.E. Kamminga, S.J. Cassidy, P.P. Jana, M. Elgaml, N.D. Kelly, S.J. Clarke, Intercalates of Bi_2Se_3 studied in situ by time-resolved powder X-ray diffraction and neutron diffraction, Dalton Trans. 50 (2021) 11376–11379, https://doi.org/10.1039/d1dt00960e.
[38] K. Osada, S. Bae, M. Tanaka, H. Raebiger, K. Shudo, T. Suzuki, Phonon Properties of Few-Layer Crystals of Quasi-One-Dimensional ZrS_3 and $ZrSe_3$, J. Phys. Chem. C 120 (2016) 4653–4659, https://doi.org/10.1021/ACS.JPCC.5B12441.